The Astronomical Journal, 136:197–211, 2008 July doi:10.1088/0004-6256/136/1/197


# HiRes DECONVOLUTION OF *SPITZER* INFRARED IMAGES

T. Velusamy[1], K. A. Marsh[1,2], C. A. Beichman[1,3], C. R. Backus[1], and T. J. Thompson[1]
[1] Jet Propulsion Laboratory, California Institute of Technology, 4800 Oak Grove Drive, Pasadena, CA 91109, USA; velusamy@jpl.nasa.gov, chas@mail.jpl.nasa.gov, Charles.R.Backus@jpl.nasa.gov, and Timothy.J.Thompson@jpl.nasa.gov
[2] IPAC, California Institute of Technology, MC 100-22, Pasadena, CA 91125, USA; kam@ipac.caltech.edu
[3] Michelson Science Center, California Institute of Technology, Mail Stop 100-22, Pasadena, CA 91125, USA
*Received 2007 September 24; accepted 2008 April 9; published 2008 June 6*

## ABSTRACT

*Spitzer* provides unprecedented sensitivity in the infrared (IR), but the spatial resolution is limited by a relatively small aperture (0.85 m) of the primary mirror. In order to maximize the scientific return it is desirable to use processing techniques which make the optimal use of the spatial information in the observations. We have developed a deconvolution technique for *Spitzer* images. The algorithm, "HiRes" and its implementation has been discussed by Backus et al. in 2005. Here we present examples of *Spitzer* IR images from the Infrared Array Camera (IRAC) and MIPS, reprocessed using this technique. Examples of HiRes processing include a variety of objects from point sources to complex extended regions. The examples include comparison of *Spitzer* deconvolved images with high-resolution Keck and *Hubble Space Telescope* images. HiRes deconvolution improves the visualization of spatial morphology by enhancing resolution (to sub-arcsecond levels in the IRAC bands) and removing the contaminating sidelobes from bright sources. The results thereby represent a significant improvement over previously-published *Spitzer* images. The benefits of HiRes include (a) sub-arcsec resolution (∼0.″6–0.″8 for IRAC channels); (b) the ability to detect sources below the diffraction-limited confusion level; (c) the ability to separate blended sources, and thereby provide guidance to point-source extraction procedures; (d) an improved ability to show the spatial morphology of resolved sources. We suggest that it is a useful technique to identify features which are interesting enough for follow-up deeper analysis.

*Key words:* infrared: general – techniques: high angular resolution

## 1. INTRODUCTION

Spatial resolution plays a key role in the astrophysical interpretation of observed images in general. While the *Spitzer Space Telescope* provides unprecedented sensitivity in the infrared (IR), the spatial resolution is limited by a relatively small aperture (0.85 m) of the primary mirror (Werner et al. 2004). In order to maximize the scientific return from *Spitzer*, it is clearly desirable to use processing techniques which make the optimal use of the spatial information in the observations.

*Spitzer* images are approximately critically sampled and have a good signal-to-noise ratio (S/N). To compensate for the effect of aperture size on angular resolution the observing strategies use redundant coverage. "HiRes" deconvolution has been designed to reassemble the information from these overlapping observations into a single image with refined resolution, justified by the increased spatial frequency coverage provided by the redundancy, in conjunction with reliable knowledge of the point-spread functions (PSFs).

The spatial resolution of an observed (or mosaicked) image is limited by diffraction to approximately $1.22\lambda/D$, based on the Rayleigh criterion which corresponds to 2.″4 at 8 $\mu$m. Deconvolution of the system point-spread response function (PRF) can improve the situation, resulting in a resolution of approximately $0.75\lambda/D$ in the limit of large S/N in the absence of additional information. However, if *a priori* information about the true image is available, further resolution improvement is possible. One readily available piece of *a priori* information is the positivity of intensity, which, when used as a constraint within the formalism of maximum likelihood estimation, enables a resolution of approximately $0.4\lambda/D$ at reasonable values of the S/N. This represents an improvement by a factor of 3 over that available in an unprocessed *Spitzer* image, and corresponds to 0.8″ at 8 $\mu$m. An optimal procedure for deconvolution in conjunction with a positivity constraint is the Richardson–Lucy (RL) algorithm (Richardson 1972; Lucy 1974), whose implementation normally involves an input image which is regularly sampled on a rectangular grid. Extension of the RL procedure to a nonuniform or irregularly-sampled grid led to the maximum correlation method (MCM) described by Aumann et al. (1990), an algorithm which formed the basis of the standard technique for resolution enhancement of *IRAS* images, and which is often referred to as "HiRes." The MCM algorithm fundamentally conserves flux at each iteration (Cao et al. 1997; J.W. Fowler 2005, private communication).

The application of HiRes to *IRAS* data provided a considerable boost to the scientific harvest of *IRAS*. As an illustrative example, in a study of the Serpens star-forming cloud core by Hurt & Barsony (1996), the unprocessed *IRAS* images (45″ × 279″ at 25 $\mu$m) barely resolved the core into two components. However, HiRes processing resulted in a spatial resolution of 25″ × 40″, sufficient to resolve 12 discrete sources when interpreted in conjunction with a point-source model; two of these sources were previously unrecognized protostars. The value of HiRes for identifying protostellar candidates was further underscored in a subsequent study of L1448 IRS2 by O'Linger et al. (1999).

The HiRes algorithm as applied to *Spitzer* data is discussed by Backus et al. (2005). Recently, Velusamy et al. (2007a, 2007b) have shown that HiRes deconvolution of *Spitzer* images enhances the spatial morphology of the outflows, jets, and cavities, thus providing a new insight into their structure and evolution. Here we present a description of HiRes deconvolution and examples of its performance on a variety of objects processed using the IRAC and MIPS *Spitzer* archive data using this technique. The examples include: comparison of *Spitzer* deconvolved images of WL16 and WL20 with high-resolution Keck and of

HH111 and HH300 with *Hubble Space Telescope* (*HST*) images, protostellar outflow sources (L1448, L1228), Fomalhaut debris disk, Tycho's supernova remnant, interacting galaxies (Arp 278, NGC2207), globular cluster NGC4590, and Galactic plane from the GLIMPSE II survey. Our examples utilize data from all available wavebands except the MIPS 160 $\mu$m band for which the data quality (limited by coverage and instrumental artifacts) did not warrant the application of deconvolution in most cases.

Our purpose for this paper is to show the community how HiRes deconvolution performs on *Spitzer* images for various astronomical objects. For the sake of completeness in Section 2 we present the description of the algorithm. It is not our intention to address the statistical robustness of this nonlinear algorithm as it is a technical and lengthy problem, which has been discussed to some extent in the literature (e.g., Aumann et al. 1990, and the references therein). There are a number of degrees of freedom, such as S/N, spatial frequency content, and degree of redundant coverage, not to mention source morphology. Dempster et al. (1977) provide a mathematical statistical treatment of the Estimation Maximization (EM) algorithm, although the reduction of their technical generality is difficult to reduce to the RL redundant coverage case. A thorough mathematical treatment (almost a proof) of the iterative technique of the deconvolution is given by Lucy (1974) and its Bayesian foundations are discussed by Richardson (1972).

## 2. *SPITZER* HiRes DECONVOLUTION

### 2.1. HiRes Algorithm

The algorithm is based on the MCM, reformulated to enable convolutions to be evaluated using the convolution theorem, which enables the use of fast Fourier transforms (FFTs).

Let

$D$ = acquired image
$P$ = PSF
$\tilde{P}$ = reflected PSF, $\tilde{P}(v) = P(-v)$
$f^n$ = current trial image estimate.

The PSF, as used here, represents the response of the telescope optics only, and does not include the spatial response of detector pixels on the focal-plane array. In subsequent discussion we will use the alternative term "point response function" (PRF) to refer to the full spatial response of the measurement system to a point source.

The initial image estimate is customarily set uniformly to unity. Then the single coverage RL algorithm can be described as a series of iterations shown in vectorized form as

$$f^{n+1} = f^n \frac{D}{f^n * P} * \tilde{P}, \tag{1}$$

a procedure which consists of three main steps: first, simulate acquisition of the data by convolving the current image with the PSF and create an image of correction factors by dividing the simulated data into the acquired data pixel by pixel. Second, convolve the correction factor image with the reflected PSF. Finally, apply the smoothed correction factors to the current image to produce the next estimate.

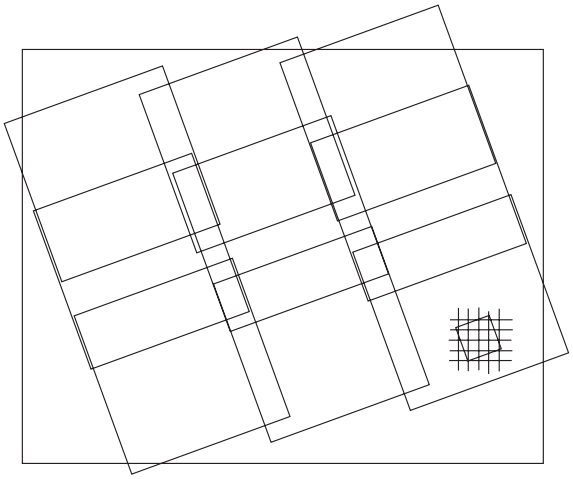

**Figure 1.** The geometry for deconvolution. Sky image, $f^n$, with partially redundant coverage by detector arrays, $D_j$ (see Equation (2)). The large tilted squares represent footprints of individual focal plane images, $D_j$. Shown in the lower right is the scale of the finer grid used to estimate the output image, the $n$th iteration of which is $f^n$, overlaid on a detector pixel whose orientation is, in general, different from that of the sky image. A given point on the sky may underlie a number of dithered image layers.

Extension to the multiple coverage case involves what is essentially weighted averaging

$$f^{n+1} = f^n \frac{\sum_j \left[\dfrac{D_j}{f^n * P_j}\right] * \tilde{P}_j}{\sum_j U_j * \tilde{P}_j}, \tag{2}$$

where $U_j$ is a unit 2D pulse function co-aligned with the $j$th data pixel.

The extension retains the key attributes of the RL method, such as flux conservation and the non-negativity of the estimated image. Our implementation makes the following two assumptions:

1. *Isoplanatic PSF.* The PSF does not vary over the detector array. The $D_j$ could be decomposed into sub-arrays small enough to assume needed stationarity with a different PSF on each one, but HiRes presently does not handle separate PSFs.
2. *Constant measurement noise.* HiRes assumes that the rms measurement error of each pixel in each observation is constant. Noise weighting each pixel would, however, be feasible, as in Aumann et al. (1990), by dividing each term in the summations by $\sigma_j^2$.

### 2.2. HiRes Implementation

We have implemented HiRes in a form which is suitable for combining multiple *Spitzer* basic calibrated data images (BCDs) onto an oversampled grid (typically 1″ for MIPS and 0.″25 for IRAC) and corrects internally for the effect of focal-plane distortion based on the distortion parameters present in the input FITS headers. It is tolerant of missing data (caused, for example, by cosmic ray hits) since the MCM does not require regular sampling of the input images. Since we do not have reliable PSFs we use PRFs (defined as as a cross-correlation of the detector pixel by the PSF) derived from observations. With some computational care the algorithm is modifiable to provide the optional use of PRFs in place of PSFs.

The geometry for the deconvolution is illustrated in Figure 1 showing the overall setting for the calculations, using

Equation (2). The trial image is sampled at a level appropriate to the amount of redundant coverage. The data images are generally not aligned with the trial image, and they are not necessarily co-aligned with each other, although for a given *Spitzer* observation set taken on the same day they would be co-oriented to within one degree of rotation. In this case it is important to note that equal (or nearly equal) $\tilde{P}_j$ can be factored out of partial sums, greatly reducing the number of FFTs that need to be performed. The same is true for the simulation convolutions: resampling to the detector image resolution and division into each member of a co-aligned subset of the $D_j$ can be performed using the trial image convolved once with one of the $P_j$ oriented with the subset.

The iterative procedure itself is a relatively simple implementation. HiRes performs various calculations to prepare for it.

1. *Resampling.* Striping is mitigated by correcting accumulations with ratios computed from pixel areas and inclusion counts.
2. *Edge effects.* Abrupt flux transitions at the image boundary can cause high frequency-ringing artifacts. We mitigate this by adopting the included PSF solid-angle weighting technique discussed in Aumann et al. (1990).
3. *Projection calculation.* Some observation scenarios can cover as much as 4 degrees of sky, mandating an exact calculation to perform tangent plane transfers. This is done with 3D homogeneous linear coordinate transformations followed by renormalization to the destination tangent plane.
4. *Distortion. Spitzer* optical distortion is recorded in the form of FITS keywords giving coefficients for quadratic or cubic bivariate Taylor series. These polynomials need to be evaluated for each trial image pixel for each observation image to determine pixel inclusions for resampling. We use the recursive Horner algorithm (published by him in 1819, but known to the Chinese hundreds of years beforehand). It involves successive factorizations of the independent variable to reach a form with nested multiplications (familiar to most students of computer science), which we generalized to the multivariate case with a second recursion on the coefficients, which in this conception are themselves polynomials, with the number of variables reduced by one. The Jacobian of the distortion transformation is needed because pixel areas in *Spitzer* images can vary by as much as 10%.

For FFTs a suitable convolution pad is added to the trial image. Then dimensions are further increased slightly, up to the nearest higher numbers which are products of powers of the first few primes. A substantial percentage of the execution time is spent evaluating the Fourier transforms, which are RAM and CPU intensive. We use as much memory as we can and use an FFT package that supports threading.

All of the image files used are in the FITS format. The program is invoked with a script run in background mode, and information about its progress is piped to a log file. Various switches set output image registration, resolution, dimensions, and orientation, the latter being important in cases where coverage is long and narrow, and diagonal to the local celestial frame. The trial images and correction factor images from successive iterations can be examined with an FITS viewer during execution. Correction factor images are useful for diagnosis of bad input pixels and poorly-matched PRFs. At convergence they should uniformly be within a percent or so of all 1s. Our largest runs, 4096 × 4096 pixel trial image and 300 256 × 256 input images, take 5 min per iteration on a modern 2 CPU PC with 2 GB of RAM running Linux.

The number of iterations to run is an imposition of *a priori* knowledge on the part of the user. The literature is extensive on stop rules for RL (see Prasad 2002). In the limit of a large number of iterations, the HiRes output image may be regarded as a maximum likelihood solution to the sky intensity distribution, subject to the constraints of non-negativity and flux conservation. However, the maximization of the likelihood occurs only after convergence is achieved. At each iteration prior to convergence, there is an implicit smoothness bias in the estimated image, and this smoothness decreases as the iterations progress. The optimal termination point for the iterative procedure then occurs when the PRF-convolved estimated image is able to reproduce the observed data to within the error bars of measurement. For the *Spitzer* data, we have found that this condition is typically achieved after approximately 50 iterations.

## 3. DATA ANALYSIS AND RESULTS

We reprocessed the raw data from *Spitzer* archives, using a version of HiRes deconvolution developed for *Spitzer* images by Backus et al. (2005). We use the BCD FITS images and SSC PRFs as input to HiRes. For all IRAC PRFs we are using the extended (about 128 detector pixels in each direction) version from SSC (contributed by Tom Jarrett). For MIPS 24 $\mu$m we use the PRF provided by the SSC in the MOPEX software package. For MIPS 70 $\mu$m we use a PRF derived by us using calibration observations of Sirius; it has better spatial coverage than the corresponding SSC PRF. The major processing steps include. (i) Download all BCDs in the selected Astronomical Observation Requests (AORs) and in preparation for HiRes preprocess data in each BCD contaminated by saturation, column pulldown, muxbleed, muxstriping, jailbars, outliers etc, using the SSC and contributed software. In the case of MIPS we do not use the BCDs with saturated pixels. However in the case of IRAC we can use them if the data were taken in a high dynamic range mode. In that case we replace saturated pixels in the long-exposure BCDs using the unsaturated data from the short-exposure BCDs. (ii) Remove background. In the RL algorithm the best-resolution enhancement is attained when the background is zero, since the source intensity above the background is then constrained to be positive, and this positivity represents a powerful piece of prior information to guide the deconvolution process. A related consequence of background removal is the reduction in "ringing" artifacts around bright point sources. The background is handled as follows: make a mosaic image of all BCDs. Perform median filtering with size 128 × 128 detector pixels to derive a background image. This background image is subtracted from the individual BCDs and negative pixel values are set to zero. We use the background subtracted BCDs as input to HiRes. The background image is later added to the HiRes image if required. Our experience so far is that background is not a serious issue for HiRes. This process preserves all large-scale features in the outflow sources. (iii) The output of our analysis for each object includes.

1. HiRes deconvolved FITS images at selected iterations;
2. HiRes uncertainty image;
3. corresponding mosaic image;
4. corresponding mosaic uncertainty image;
5. corresponding mosaic coverage image.

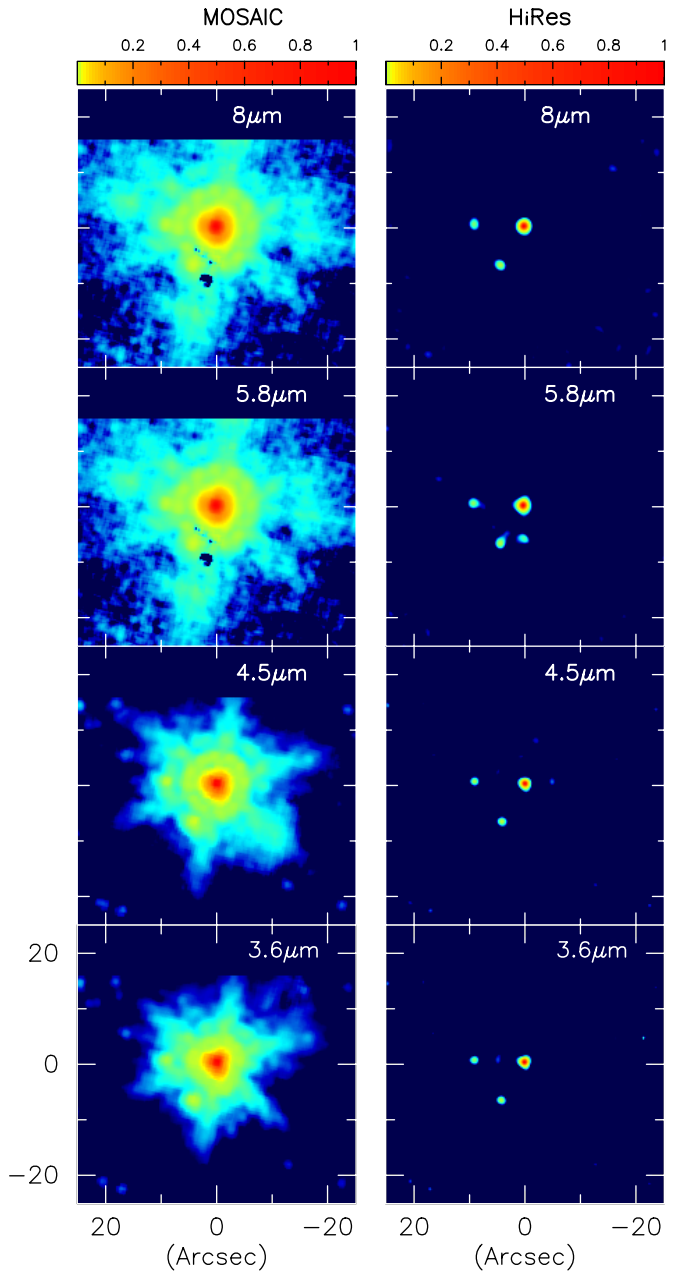


**Figure 2.** Point-source responses of the IRAC bands. The mosaic (left) and HiRes deconvolved (right) images of a star observed in the field of B335. Intensities are normalized to unity at the peak. Identical square-root color stretch is used for all bands for both mosaic and HiRes images. The (0, 0) position is R.A.(2000):19:36:57.12; decl.(2000):+07:35:23. Two faint point sources (to the east and south–southeast of the bright source) inside diffraction lobes appear clearly in the deconvolved images.

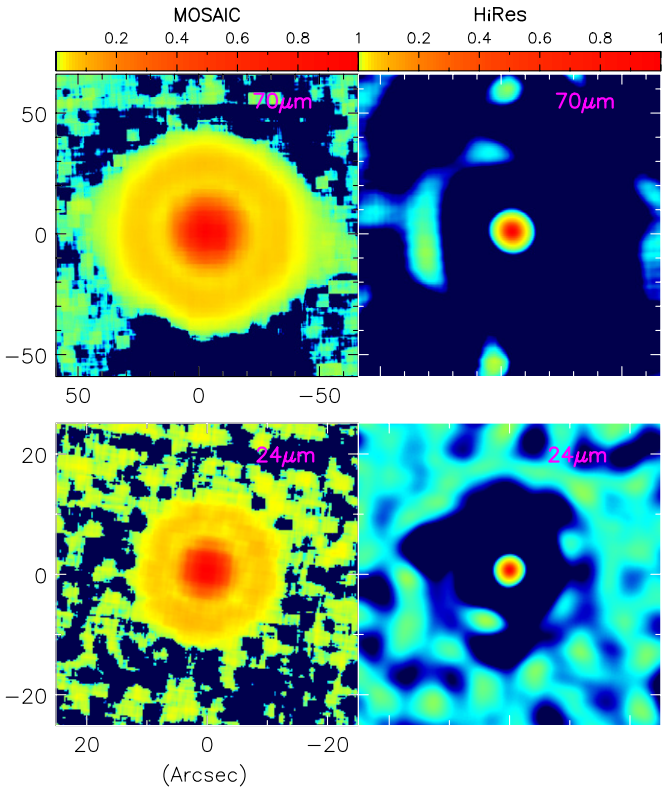


**Figure 3.** Point-source responses of the IRAC bands. The mosaic (left) and HiRes deconvolved (right) images of a point source observed in the field of B335. Intensities are normalized to unity at the peak. Identical square-root color stretch is used for all bands for both mosaic and HiRes images. The 24 $\mu$m images are for the same source shown for IRAC (Figure 2). The 70 $\mu$m images are for the B335 protostar.

In HiRes we used 50 iterations for the IRAC bands and 100 for MIPS, which resulted in a FWHM of 0.55″–0.75″ for IRAC channels 1–4 and 1.6″ at 24 $\mu$m for a point source in the deconvolved images. All bands are relatively free of artifacts except the IRAC channel 4 (at 8 $\mu$m) which often shows streaks due to uncorrected muxbleed. In the HiRes images diffraction residuals near the Airy rings are low at a level <0.05% of the respective peak intensities at 3.6, 4.5, and 5.8 $\mu$m, providing enhanced visualization of the high- and low-surface brightness closer to the bright sources.

It is important to use an appropriate PRF, since a PRF mismatch results in poor performance of the deconvolution (large diffraction residuals). Our implementation of HiRes was initially delayed by the lack of availability of suitable PRFs—the early ones from SSC were not suitable for deconvolution as the mismatch produced substantial artifacts in the images. HiRes enables the combining of data from multiple epochs: the BCDs obtained at different epochs are combined taking into full consideration the PRF orientation on-sky. In mosaic images the sidelobe orientations may differ with epochs and thus in a multi-epoch mosaic image the point sources may not match the PRFs.

### *3.1. HiRes on a Point Source*

The demonstrations shown in Figures 2–4 and the values in Tables 1 and 2 describe the performance of HiRes deconvolution on a bright point source. For this demonstration we use a bright star (at position R.A., decl. (2000): 19:36:57.12 +07:35:23) about 93″ to the NE of the B335 protostar. At MIPS 70 $\mu$m this star is too weak and we use the B335 protostar itself to characterize the point-source response in the HiRes image. In Figures 2 and 3 we show the HiRes images and the corresponding mosaic images. We used identical color stretches for both the HiRes and mosaic images to bring out the weakest emission in the diffraction lobes. It may be noted that in the IRAC images at low brightness levels (less than 1% of the peak brightness of the star) there are two point sources within ∼9″ from the star. In the mosaic images they are swamped by the diffraction lobes. HiRes deconvolution achieves sub-arcsec resolution for the IRAC bands. The FWHM values obtained by Gauss fit to the bright star are shown in Table 1 and Figure 4.

**Table 1**
Point-Source FWHM in Mosaic and HiRes Images in Figures 2 and 3

| Band | FWHM | HiRes FWHM (arcsec) | | | | |
|---|---|---|---|---|---|---|
| $\lambda(\mu m)$ | mosaic | 3 iterations | 10 iterations | 30 iterations | 50 iterations | 100 iterations |
| IRAC 3.6 | 1.79 × 1.94 | 1.76 × 1.78 | 1.06 × 1.01 | 0.74 × 0.66 | 0.62 × 0.54 | 0.49 × 0.42 |
| IRAC 4.5 | 1.91 × 2.02 | 1.56 × 1.48 | 0.95 × 1.02 | 0.68 × 0.63 | 0.51 × 0.56 | 0.39 × 0.42 |
| IRAC 5.8 | 2.30 × 2.40 | 1.91 × 2.06 | 1.24 × 1.37 | 0.84 × 0.93 | 0.69 × 0.78 | 0.53 × 0.60 |
| IRAC 8 | 2.34 × 2.30 | 2.04 × 2.19 | 1.31 × 1.41 | 0.85 × 0.92 | 0.69 × 0.76 | 0.51 × 0.57 |
| MIPS 24 | 5.75 × 5.87 | 5.05 × 5.12 | 3.35 × 3.42 | 2.25 × 2.33 | 1.85 × 1.92 | 1.40 × 1.47 |
| MIPS 70 | 18.9 × 18.1 | 17.6 × 16.7 | 9.2 × 11.5 | 10.9 × 7.8 | 7.5 × 6.1 | 5.5 × 4.8 |

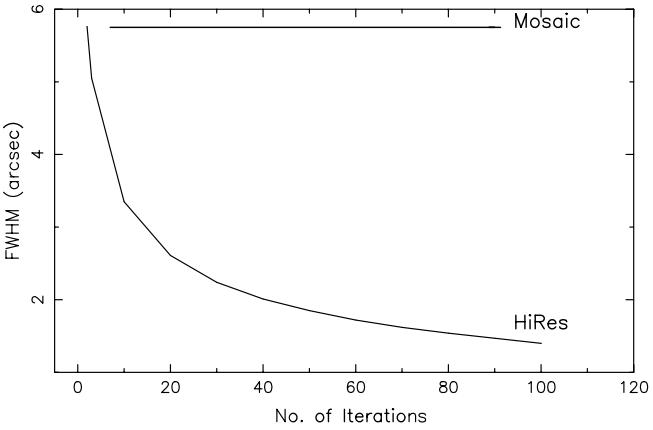


**Figure 4.** The FWHM of a point source in the MIPS 24 $\mu$m HiRes images as a function of the number of iterations. For comparison the FWHM in the mosaic image is also shown.

**Table 2**
Diffraction Residual Levels (Normalized to the Peak Brightness) at the Airy Rings in Mosaic and HiRes Images

| Band $\lambda(\mu m)$ | Mosaic | HiRes | Ref |
|---|---|---|---|
| IRAC 3.6 | $9.2 \times 10^{-3}$ | $6.7 \times 10^{-4}$ | Figure 12 |
| IRAC 4.5 | $6.0 \times 10^{-3}$ | $4.2 \times 10^{-4}$ | Figure 12 |
| IRAC 5.8 | $5.0 \times 10^{-3}$ | $6.0 \times 10^{-4}$ | Figure 12 |
| IRAC 8 | $4.0 \times 10^{-3}$ | $2.0 \times 10^{-4}$ | Figure 12 |
| MIPS 24 | $7.6 \times 10^{-2}$ | $6.2 \times 10^{-3}$ | Figure 11 |
| MIPS 70 | $7.4 \times 10^{-2}$ | $3.6 \times 10^{-3}$ | Figure 11 |

Table 1 shows the typical resolution enhancement in the HiRes images over the corresponding mosaic images. The exact values for the FWHM in a given set of images may differ marginally depending on the number of BCDs (map pixel coverage). However we do not see any significant variations above 10%. In Table 2 we show the level of diffraction residuals observed at Airy rings in some of the HiRes images. To give a conservative estimate we have chosen the images that displayed somewhat high residuals as indicated. A comparison of the mosaic and deconvolved images show that diffraction lobes are removed to a very high degree. In the diffraction residue in the deconvolved images a low-level ringing around bright point sources is seen at levels indicated in Table 2. These are at levels lower than diffraction lobes in the mosaic images by factors of $>10$. It may be noted that these are conservative estimates obtained using the images as indicated in the table rather than using the best cases in our analysis. Removing the diffraction structures to such low levels more clearly brings out the morphology of the faint emission around bright objects.

We have verified via extensive numerical calculations with both synthetic and real data that the resulting enhancement in angular resolution is approximately three times that obtainable

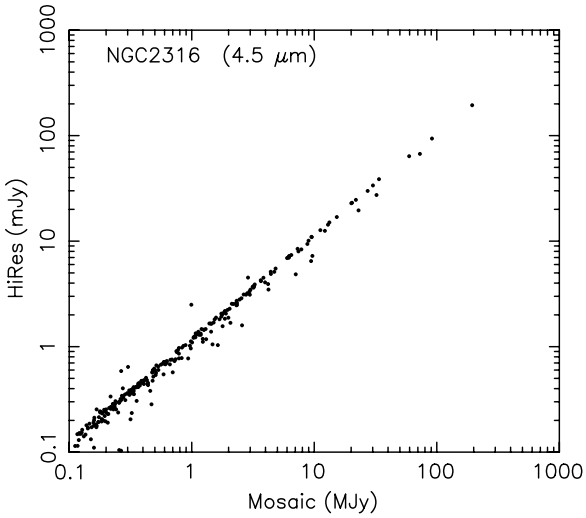


**Figure 5.** HiRes fluxes compared with those extracted from mosaic images. The fluxes are taken from the results for the cluster NGC2316 (Langer et al. 2007). The source extraction and photometry were made using SExtractor.

in raw co-added (mosaic) images, and that the fluxes of individual point sources are conserved to a level that is better than 5%. In Figure 5 we show a comparison of the HiRes fluxes with those extracted from mosaic images for a young cluster NGC2316 (Langer et al. 2007).

## 4. RESULTS OF HiRes IMAGE ENHANCEMENT FOR SELECTED ASTRONOMICAL OBJECTS

In this section we show examples of HiRes deconvolution on a variety of objects so chosen to give a general feeling on the performance of HiRes and its usefulness for the specific class of objects and science goals. The results presented here are limited to highlighting the performance of the deconvolution technique rather than to providing detailed scientific objectives and consequences. The images are presented most often using a square-root scale and color stretches. The color stretches used are similar in all images and the colors represent the relative intensities as indicated by the wedges shown in some figures. The number of iterations of the HiRes images shown is 50 if not indicated otherwise.

### *4.1. Comparison with Keck High-Resolution Images*

To fully demonstrate the robustness of the deconvolved features we compare the *Spitzer* HiRes deconvolved images at 8.0 $\mu$m with high spatial resolution images observed with Keck at 7.9 $\mu$m. The *Spitzer* and Keck images of a Young Stellar Object (YSO) WL 16 and a multiple star system WL 20 are shown in Figures 6 and 7, respectively. The Keck images in

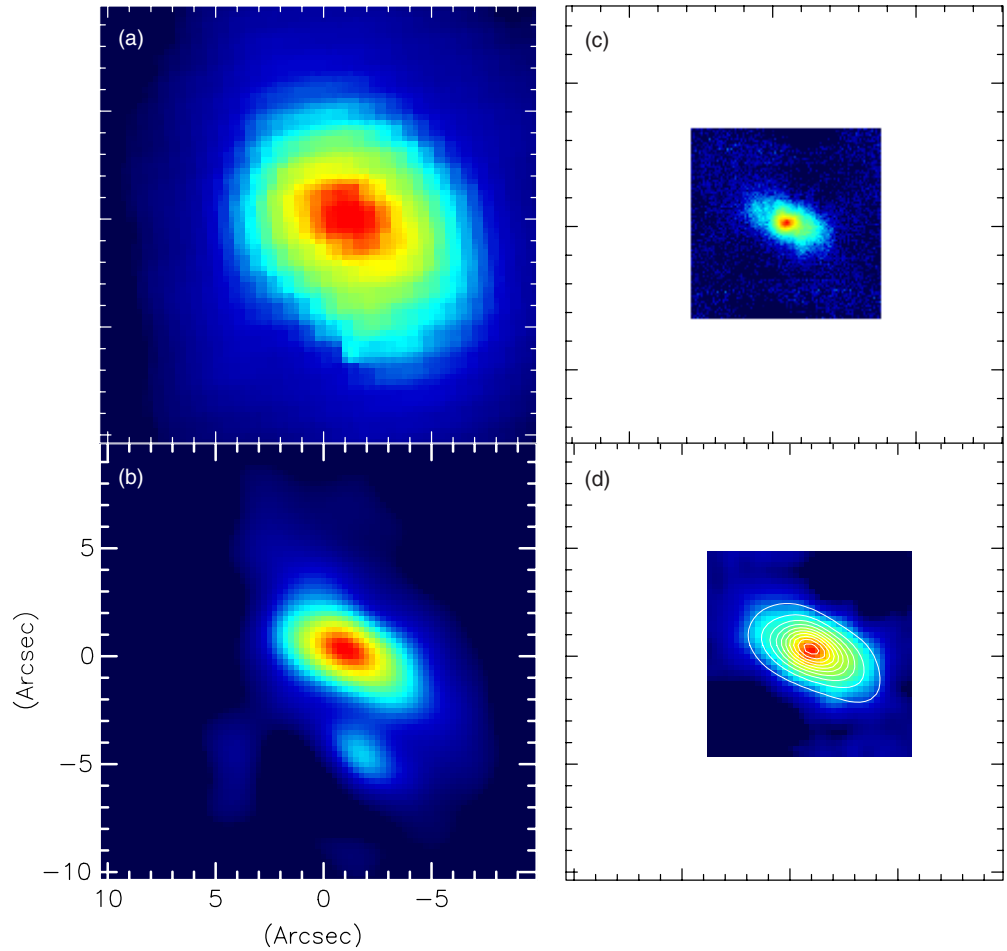


**Figure 6.** Comparison of 8 $\mu$m *Spitzer* HiRes deconvolved images with 7.9 $\mu$m Keck image of YSO WL16: (a) *Spitzer* mosaic image; (b) *Spitzer* deconvolved image; (c) full resolution Keck image; (d) contour map of *Spitzer* deconvolved image overlaid on Keck image smoothed to the resolution of *Spitzer* deconvolved image. The Keck images are generated using the data from Ressler & Barsony (2003).

Figures 6 and 7 are reproduced from Ressler & Barsony (2001, 2003). The Keck images were obtained using the JPL's mid-IR camera, MIRLIN (Ressler et al. 1994) with high spatial resolution of 0.3″. The left panels in each figure show the *Spitzer* 8 $\mu$m (a) mosaic, and (b) deconvolved images. The right panels show the Keck images (c) observed with full resolution (0.3″), and (d) smoothed to the resolution of the *Spitzer* deconvolved images. WL 16 is an embedded intermediate-mass (2–8 $M_{\odot}$) YSO in $\rho$Oph which shows polycyclic aromatic hydrocorbon (PAH) emission features (Waters & Waelkens 1998) and has a unique extended, high-surface-brightness disk which is visible only at mid-IR wavelengths. In the Keck images Ressler & Barsony (2003) observed a disk size of 7″ × 3.5″, corresponding to a disk diameter of ∼900 AU. The disk's major axis is at a position angle of 60°. These features as seen in the Keck image (Figure 6(d)) are very well represented in the deconvolved *Spitzer* image (Figure 6(b)) demonstrating the fidelity of deconvolution for imaging extended morphology. The *Spitzer* contour map overlaid on the Keck image (Figure 6(d)) brings out the excellent agreement between the two images. A low intensity blob seen at ∼5″ to the south in the Spizer deconvolved image is not an artefact produced by the deconvolution and its presence in the original data is evident in Figure 6(a).

WL 20 is classified as an "IR companion system," with WL 20 S exhibiting an embedded protostellar (Class I) spectral-energy distribution (SED) while its two neighbors, WL 20 E and W, each exhibit a T Tauri star (Class II) SED (Ressler & Barsony 2001). The IR companion, WL 20 S, is the dominant luminosity source in the system. The components W20 S and W are blended in the *Spitzer* mosaic image and they are fully deblended in the HiRes deconvolved image. It may be noted that we used 100 iterations for this deconvolution as it deblended the sources more clearly than using the nominal 50 iterations. The *Spitzer* deconvolved 8 $\mu$m image (Figure 7(b)) is in excellent agreement with the Keck 7.9 $\mu$m image (Figure 7(d)). The *Spitzer* 8 $\mu$m flux densities of the components S, E, and W measured using the deconvolved images are 200.6, 153.1, and 47.6 mJy, respectively compared to the Keck 7.9 $\mu$m fluxes 123.0, 121.0, and 38.4 mJy, respectively (Ressler & Barsony 2001). The differences in the absolute and relative flux densities may be due to (i) possible differences in the flux calibrations, and (ii) the broader bandwidth by a factor >2 for *Spitzer* 8 $\mu$m than for Keck data, considering the fact the SEDs for components E and W show strong decrease in flux with increasing wavelength while component S shows increasing flux with wavelength (Ressler & Barsony 2001).

### *4.2. Protostellar Outflows*

The young protostellar objects are so heavily obscured at visual wavelengths that their disks, outflows, and envelopes cannot be observed directly. The *Spitzer* IRAC and MIPS bands offer a unique opportunity to study protostars, protostellar

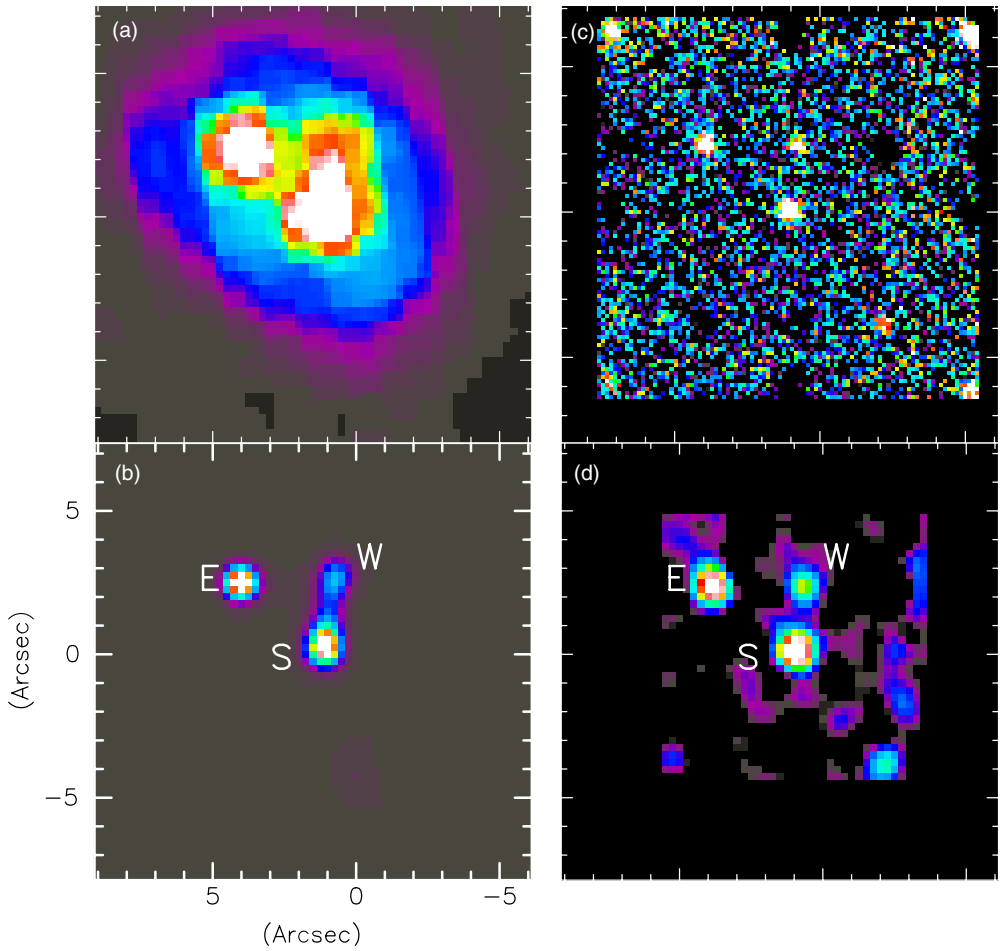


**Figure 7.** Comparison of 8 $\mu$m *Spitzer* HiRes deconvolved images with 7.9 $\mu$m Keck image of a triple companion system WL20: (a) *Spitzer* mosaic image; (b) *Spitzer* deconvolved image; (c) full resolution Keck image; (d) Keck image smoothed to the resolution of *Spitzer* deconvolved image. The Keck images are generated using the data from Ressler & Barsony (2001).

disks, outflows, and protostellar envelopes and cores. In short-wavelength IRAC bands the outflow cones are observable in scattered light from the protostar through the cavity created by the jets and outflows (Tobin et al. 2007; Velusamy et al. 2007a, 2007b). The emissions in the IRAC bands are also considered to be from the the $H_2$ rotational lines and possibly some contribution from PAHs (e.g. Noriega-Crespo et al. 2004a, 2004b; Neufeld et al. 2006). Recently Velusamy et al. (2007a) have shown that molecular jets and molecular gas in the bow shocks are observable in the IRAC bands while the hottest atomic/ionic gas in the bow shocks, are observable in the MIPS 24 $\mu$m band from the atomic/ionic line emissions. The dust emission from the protostar in the MIPS bands are good diagnostics of the circumstellar disks. However these low-surface-brightness features can be severely confused by the high brightness of the protostar and the disk. Deconvolution removes, or at least minimizes, the diffraction effects of the brightest features enabling improved visualization of the low-surface features around them. Furthermore, the resolution enhancement provides a sharper view of the outflow cavity walls, molecular jets and bow shocks.

#### *4.2.1. Comparison with HST NIRCAM2 images*

In this section we present the HiRes deconvolved *Spitzer* images of two outflow objects HH111 and HH300 at 3.6 $\mu$m and compare them with the high-resolution *HST* images at a closest wavelength of 2.2 $\mu$m observed by Reipurth et al. (1999) with the NICMOS2 camera (NIC2). The *Spitzer* and *HST* images of HH111 and HH300 are shown in Figures 8 and 9. The left panels in each figure show the *Spitzer* 3.6 $\mu$m (a) mosaic, and (b) deconvolved images. The right panels show the *HST* NIC2 F205W images (c) observed with full resolution ($\sim$0.3″), and (d) smoothed to the resolution ($\sim$0.65″) of the *Spitzer* deconvolved images. The protostar locations are marked by the arrows. The relative faintness of the protostars in the NIC2 image is due to heavy circumstellar obscuration. In both objects the reflection nebulosities (scattered light from the protostars) delineate the wide-angle outflow cavities around the protostars. The outflow morphologies are not at all evident in the *Spitzer* mosaic images, but are brought out more clearly in the HiRes deconvolved images due to both the increased resolution and the reduced sidelobe levels.

HH111 shows a complex reflection nebula possibly due to the presence of two protostars. A second protostar "B" is observed in the *HST* and *Spitzer* images $\sim$3″ further to the west, which appears to contribute significantly to the illumination of the blueshifted outflow cavity of the HH 111 protostar "A" (Reipurth et al. 1997). The outflow lobes of HH111 (protostar "A") are roughly in the east–west direction and its eastern lobe is seen clearly without confusion from that of star "B." However, the simple outflow cone morphology of the western lobe is complicated by the north–south outflow lobes from the star "B." Considering the differences in their wavelengths and the brightness of the protostars between the

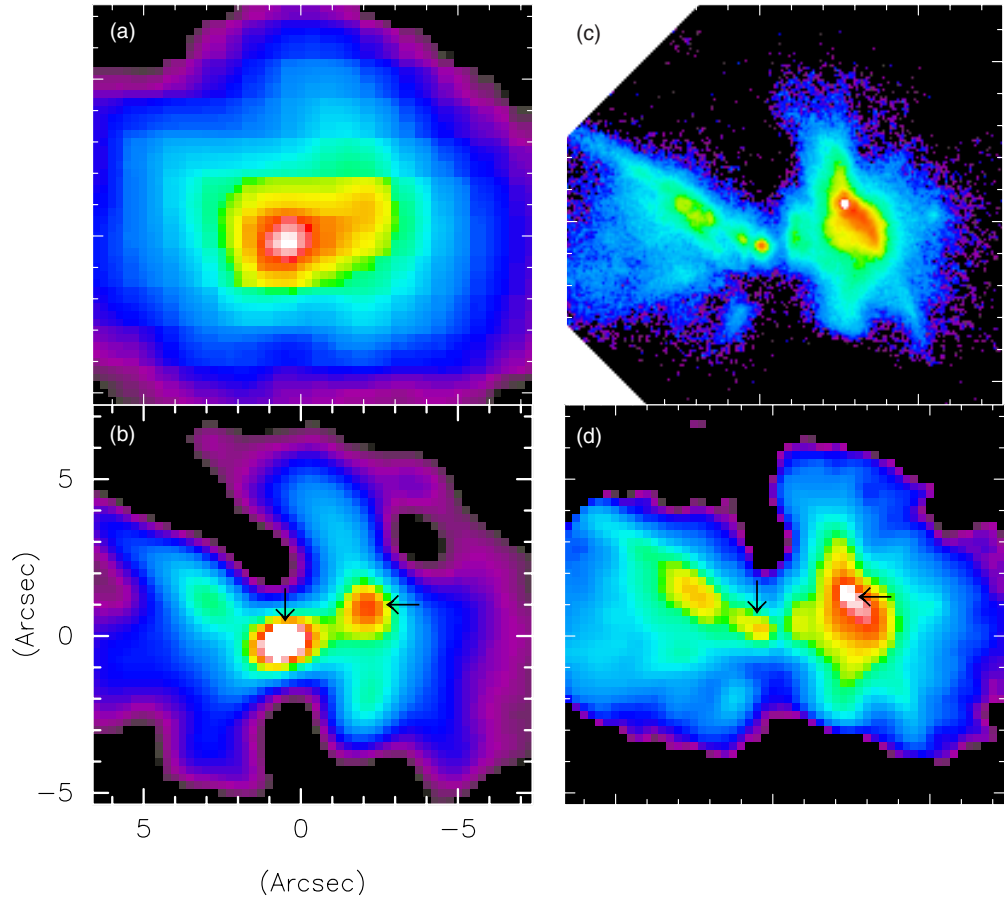


**Figure 8.** Comparison of 3.6 $\mu$m *Spitzer* HiRes deconvolved image with *HST* NICMOS2 image of HH111: (a) *Spitzer* mosaic image; (b) *Spitzer* deconvolved image; (c) full resolution *HST* NIC2 F205W image; (d) NIC2 image smoothed to the resolution of *Spitzer* deconvolved image. The black arrows mark the protostar. The *HST* images are generated using the data from Reipurth et al. (2000).

*HST* NIC2 (Figure 8(d)) and *Spitzer* images (Figure 8(b)) we find that the HiRes deconvolution has retained a high fidelity preserving all the main features observed in the *HST* image.

In the *HST* image of HH300 (Figure 9(c)) a bright cometary reflection nebula surrounding the protostar is observed (Reipurth et al. 2000). The reflection nebula is remarkably symmetric about the jet axis toward the northeast from the protostar, representing the outflow lobe seen by scattered light from the star. Despite the diffraction pattern, it is clear that the reflection nebula shows part of the southwest lobe structure close to the star. The *Spitzer* mosaic image (Figure 9(a)) is dominated by the diffraction lobes of the bright protostar and there is only a slight hint of the presence of the northeast lobe. However, reducing the levels of the diffraction lobes with HiRes deconvolution it has been possible to bring out its presence more clearly. It may be noted that in this example we have used only 20 iterations, fewer than the nominal 50. Use of 50 iterations tends to break up the extended low-surface-brightness structure of the outflow lobe. The diffraction residue is present at a visible level but still low enough to bring out the underlying outflow morphology. It may be noted that the star is so bright that it was close to saturation in the data used for this image. (It was saturated in a number of BCDs of this region.) The choice of using 20 iterations at the expense of sacrificing resolution enhancement (see Figure 4) seems more appropriate for extended structures while with larger iterations deconvolution performs better for point sources and small-scale structures.

HH300 shows an example where HiRes deconvolution has been marginally successful in bringing out the extended structure around very bright point sources. In cases such as L1228 (Figure 13(a)) the deconvolution failed to bring out the low brightness wide-angle outflow morphology due to the presence of large levels of diffraction residue. Mismatches between the PRF and point-source image can result in large diffraction residue in the deconvolved image, especially when the sources are very bright, close to saturation, and they are not represented well by the PRF. On the other hand the HiRes deconvolution successfully brought out the outflow cone morphologies in L1448 IRS2 (Figure 11) where the protostar was not too bright.

#### *4.2.2. Outflows in L1448-IRS2*

Tobin et al. (2007) presented deep IRAC images that highlight the scattered light emission around many of the youngest protostars, the so-called Class 0 sources, in L1448. Here we present the results of HiRes processing of the IRAC and MIPS images. Figure 10 shows the IRAC 4.5 $\mu$m images of the full field containing L1448 mm, IRS2, and IRS3 and their large-scale jets and outflows. Note that the diffraction residuals around the bright stars in this field are negligible in the HiRes image. The marginal Airy ring residuals around the brightest star in the eastern edge of the image are due to the fact that this star is too bright and close to saturation. In Figure 11 we show a blow-up of the IRS2 protostar and outflow in all IRAC and MIPS 24 and 70 $\mu$m.

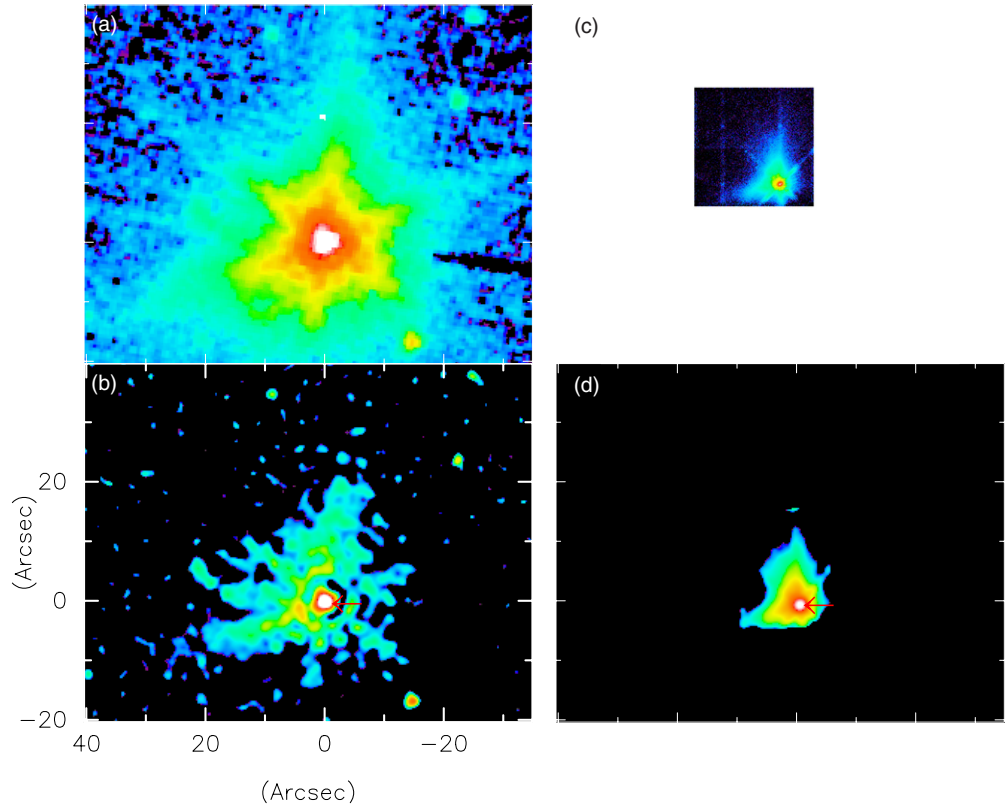


**Figure 9.** Comparison of 3.6 $\mu$m *Spitzer* HiRes deconvolved image with *HST* NICMOS2 image of HH300: (a) *Spitzer* mosaic image; (b) *Spitzer* deconvolved image; (c) full resolution *HST* NIC2 F205W image; (d) NIC2 image smoothed to the resolution of *Spitzer* deconvolved image. The red arrows mark the protostar. The *HST* images are generated using the data from Reipurth et al. (2000).

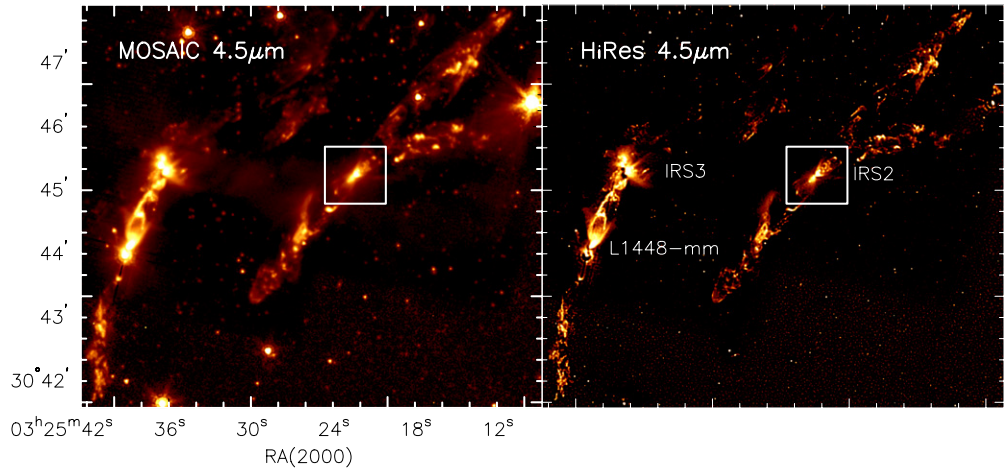


**Figure 10.** Mosaic and HiRes images of L1448 at 4.5 $\mu$m. The protostars in this field are marked. The box represents the region of IRS2 shown in detail in Figure 11.

### *4.2.3. Outflow in L1228*

L1228 is a well-studied system with a wide-angle CO outflow and molecular $H_2$ jets. This object formed part of our HiRes analysis of First Look Survey (FLS) data and its results demonstrate the performance of the deconvolution on a star close to saturation. HiRes results are shown in Figures 12 and 13. In the mosaic images the emission around the protostar is overwhelmed by the diffraction lobes from the bright protostar. In the HiRes images the diffraction residuals are significantly low to bring out the features associated with the molecular jet. In Figure 13 we show a three-color image of IRAC emission and for comparison we reproduced the CO and $H_2$ molecular jets, from Arce & Sargent (2006). The outflow cavity in scattered light is not detected in the IRAC images presumably due to lower density in the envelope. The emissions at 4.5 $\mu$m as well as other IRAC bands show good correlation with the $H_2$ jet (seen as a string of knots).

### *4.3. Spitzer FLS Verification Field*

The extragalactic component of the *Spitzer* FLS is composed of two parts—a large-area shallow survey covering an area of $2.5^\circ \times 2^\circ$ and a smaller $\sim 0.75^\circ \times 0.3^\circ$ strip, referred to as

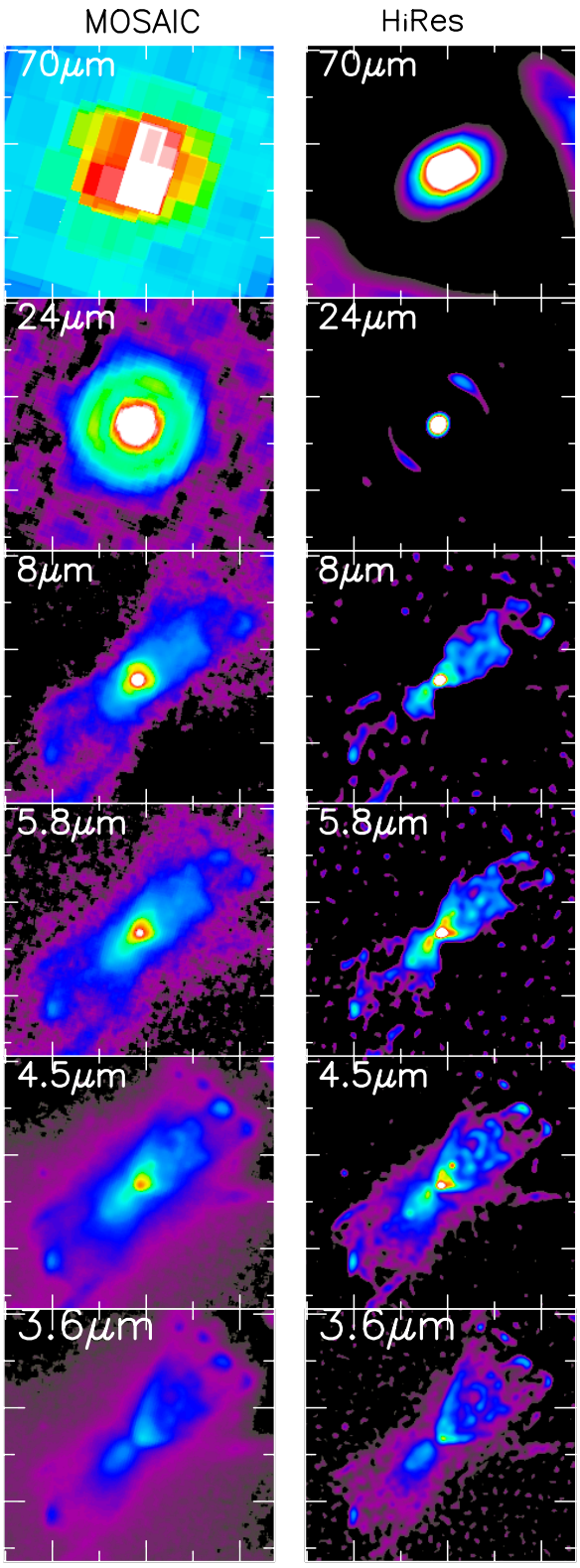


**Figure 11.** L1448 IRS2 central region (as marked in Figure 10). Panels show mosaic and HiRes images of L1448 IRS2 in IRAC and MIPS bands.

the verification survey (or FLSv) (see Frayer et al. 2004). Fryer et al. discuss the *Spitzer* counterparts in Very Large Array (VLA) and WSRT-FLSv sources (Condon et al. 2003; Morganti et al. 2004) representing radio selected Submillimeter Galaxies (SMGs). In Figure 14 we show the MIPS 24 $\mu$m images of their source no. 1. The HiRes deconvolution clearly presents a more clear view than the published 24 $\mu$m image (Figure 1 in Frayer et al. 2004) of the five individual component galaxies identified in the VLA/Westerbor/IRAC maps. Though the individual components are resolved in the mosaic image there is an indication of an extended envelope containing the five SMGs. However it is likely that the extended emission is the result of the sidelobes in the PRF. Indeed as demonstrated in Figure 14 HiRes deconvolution this envelope is removed gradually with each iteration as would be expected for sidelobes. At iteration 50 and above the diffraction envelope is removed entirely to the sensitivity limit and a sharper view of the components is obtained.

### *4.4. Fomalhaut Debris Disk*

The study of dusty debris disks around main-sequence stars can provide clues to the possible presence of orbiting bodies such as planets. In particular, by resolving the structures observed in the dust emission we can identify the grains trapped in various resonances caused by an unseen planet/planets around the star. One system of considerable interest is Fomalhaut (a Ps$\alpha$), which shows a ring morphology of the debris disk in submillimeter (Marsh et al. 2005) and in optical (Kalas et al. 2005) bands. The first *Spitzer* results at 24, 70, and 160 $\mu$m Early Release Observations (ERO) were presented by Stapelfeldt et al. (2004). They presented the first demonstration of HiRes deconvolution of MIPS data that was performed on the 70 $\mu$m images of Fomalhaut. Recently there have been new observations with *Spitzer*. In Figure 15 we show a new HiRes image at 70 $\mu$m that has been obtained using all the data available to date. The deconvolved image clearly brings out the pair of intensity maxima interpreted as the pericenter and apocenter of an inclined ring. The asymmetries in their intensities resulting primarily from the temperature differences and marginally due to dust column densities confirm the ringlike morphology but also show that the geometric center is displaced from the star by about 8 AU.

### *4.5. MIPS 24 $\mu$m Images of Tycho's Supernova Remnant*

In Figure 16 we show a HiRes deconvolution of the MIPS 24 $\mu$mimage of Tycho's supernova remnant. This demonstrates the fidelity of the HiRes deconvolution. A comparison of the deconvolved *Spitzer* image with *Chandra X-ray* images (Warren et al. 2005; Cassam-Chenaï et al. 2007) show that 24 $\mu$m IR emission shows an association with the blast wave, and not with the ejecta from the supernova as seen in the Kepler's supernova remnant (Blair et al. 2007). We are seeing ambient interstellar dust that has been swept up and heated by the main blast wave. The dusty grains are possibly conditionally heated by electrons in the X-ray-emitting hot gas. A combined analysis of deconvolved IR images of supernova remnants with X-ray images may provide a powerful diagnostic on plasma conditions in the remnant shells.

### *4.6. Interacting Galaxies*

The starbursts in interacting galaxies are traceable in MIPS bands and it is therefore necessary to compare MIPS images with those in the IRAC bands or optical bands. The *Spitzer* resolution in the MIPS bands are too coarse for a meaningful comparison. The HiRes deconvolved beams at 24 $\mu$m match the observed beams in the IRAC bands.

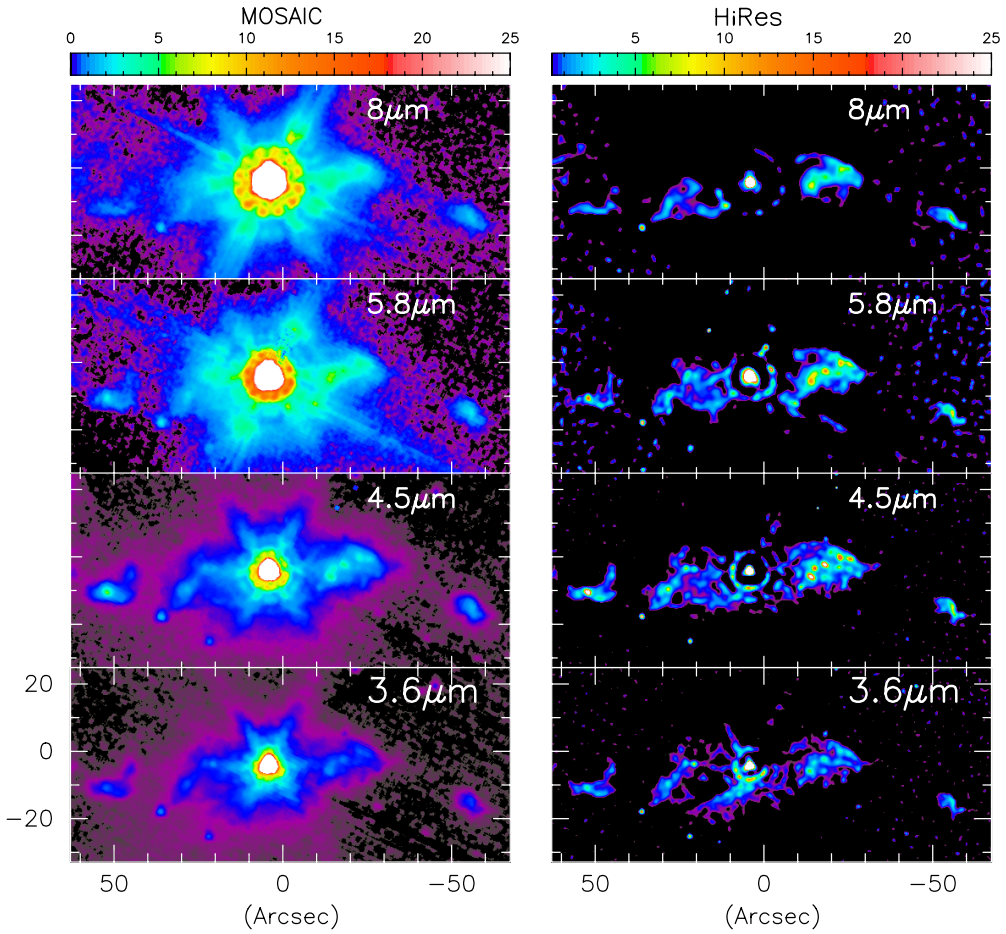


**Figure 12.** Protostar L1228. Panels show mosaic and HiRes images in the IRAC bands. The diffraction residues in the deconvolved maps are at low levels as given in Table 2.

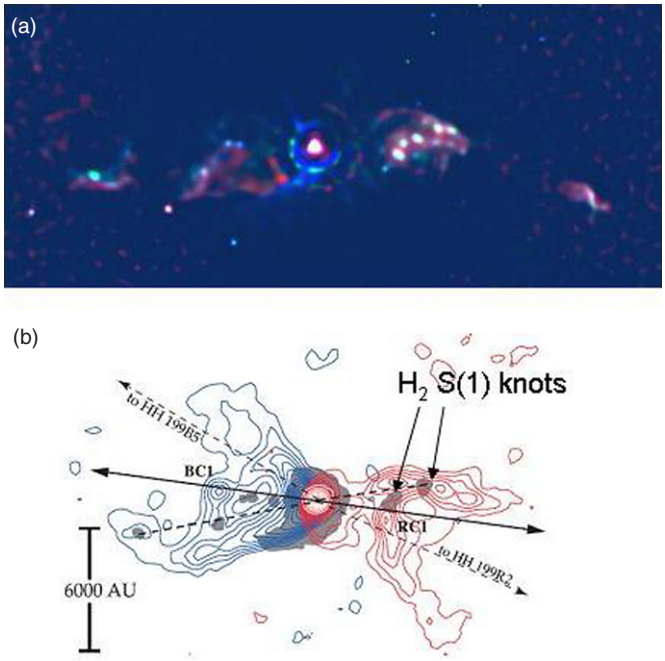


**Figure 13.** (a) IRAC three-color images of L1228. (blue: 3.6 $\mu$m, green: 4.5 $\mu$m, red: 8 $\mu$m); (b) red- and blue-shifted CO emission (contour) and 2.7 mm continuum (white contour); $H_2$ S(1) 2.122 $\mu$m emission (gray) (reproduced from Arce & Sargent 2006).

#### *4.6.1. NGC2207 & IC2163*

Elmegreen et al. (2006) presented the IRAC and MIPS observations of interacting galaxies NGC2207 & IC2163. In Figure 17 we show the IRAC 3.6 and 8 $\mu$m and MIPS 24 and 70 $\mu$m images. The HiRes deconvolution reveals detailed morphology of the interacting pair, particularly the starbursts as traced in the MIPS images. Of particular interest is the feature identified as "i" by Elmegreen et al. (2006) in the far-western edge. This is the brightest feature in the 24 and 70 $\mu$m images. This clump is also the brightest emission in $H_\alpha$ and radio continuum. The HiRes 24 $\mu$m image shows a ring-like resolved structure. Though this emission resembles the diffraction residue at the Airy rings, the emission is at a smaller radius and at a much higher level than that usually observed in point sources (Table 2).

#### *4.6.2. Arp 278*

Arp 278 (NGC7253) is a starburst-interacting galaxy pair. The HiRes 8 and 24 $\mu$m images (Figure 18) bring out the prominence of the emission along the streamers.

### *4.7. Globular Cluster: NGC4590*

In Figures 19 and 20 we show the mosaic and deconvolved images of globular cluster NGC 4590 (M68) to demonstrate how well the HiRes deconvolution deblends the stars in such a

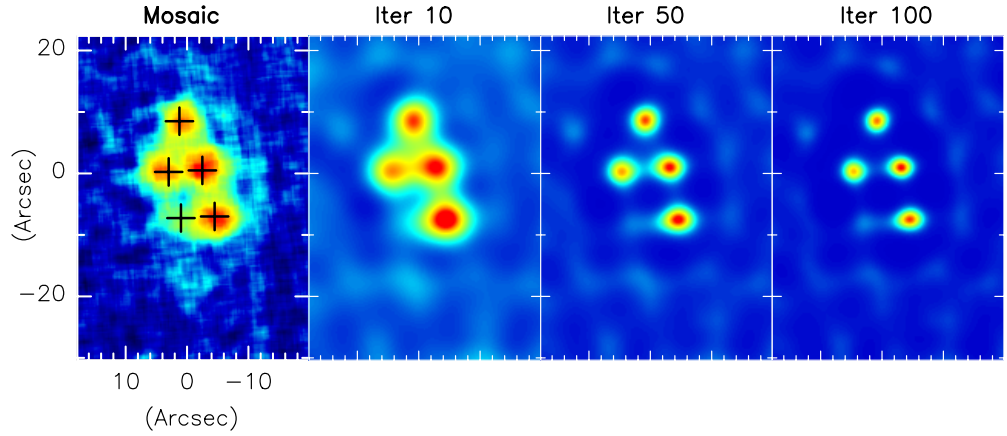


**Figure 14.** MIPS 24 $\mu$m HiRes deconvolved images of a radio-selected galaxy group in the FLSv field obtained after iterations of 10, 50, and 100 are shown along with the mosaic image. The crosses mark the position of the galaxies detected by the VLA. It also demonstrates the number of HiRes iterations versus image enhancement. Note that the envelope around these galaxies as seen in the mosaic disappears completely after 50 iterations.

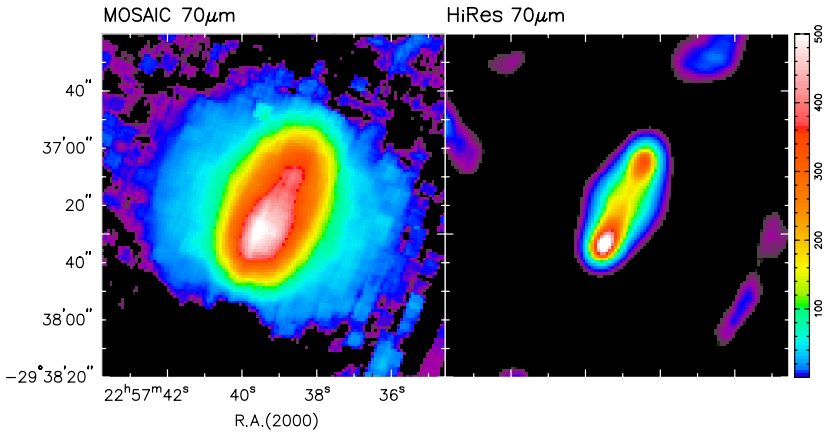


**Figure 15.** MIPS 70 $\mu$m images of Fomalhaut. The mosaic and HiRes images use all observed data in *Spitzer* archives as of 2007 May.

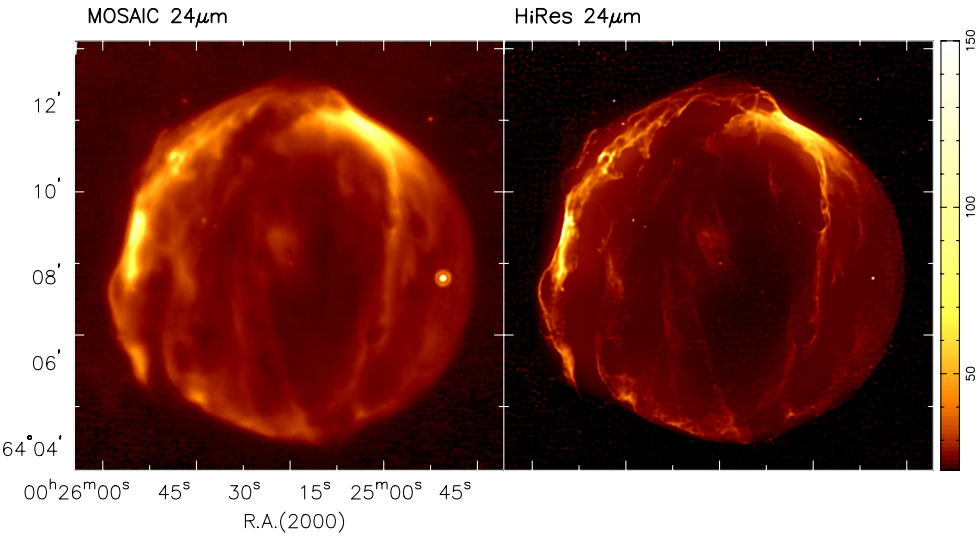


**Figure 16.** MIPS 24 $\mu$m images of Tycho's supernova remnant.

high-density region. Nearly a factor of 3 enhancement in angular resolution (9 in area) reduces the area of the Airy disk of a star in the mosaic images by a factor of 9 in the deconvolved image allowing overlapping stars to deblend very well. The IRAC three-color images clearly show the dominance of stars in the shortest wavelength (blue). In HiRes images of IRAC channel 2 and 3 we can clearly identify more stars than in the corresponding mosaic images at least by factors of 3 (see Section 3.1). All of the seven giant stars observed by Lee et al. (2005) are clearly detected in all IRAC bands. One of the stars (No. 350), closest to the cluster center is blended in mosaic images while it is clearly resolved from the neighboring objects

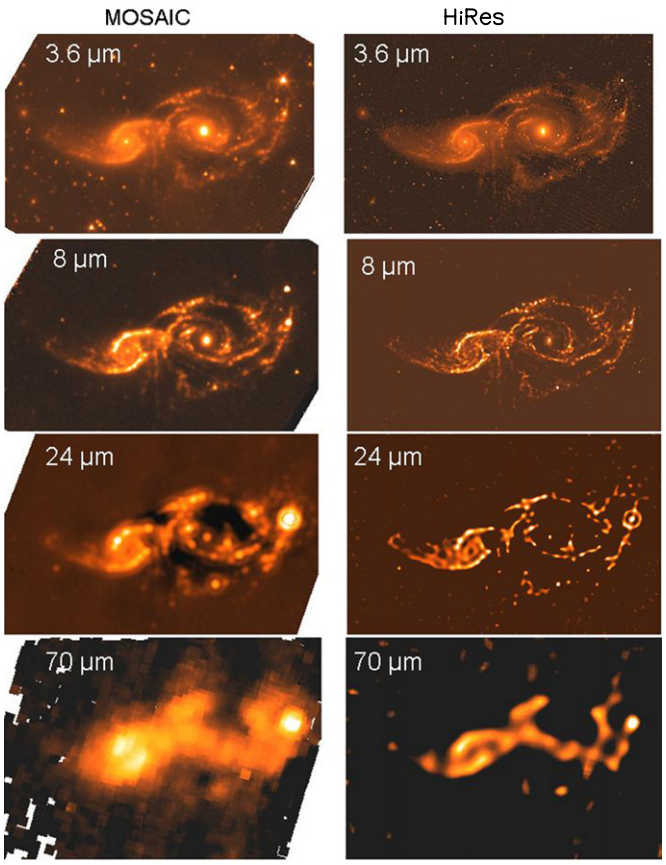


**Figure 17.** IRAC and MIPS observations of interacting galaxies NGC2207 and IC2163.

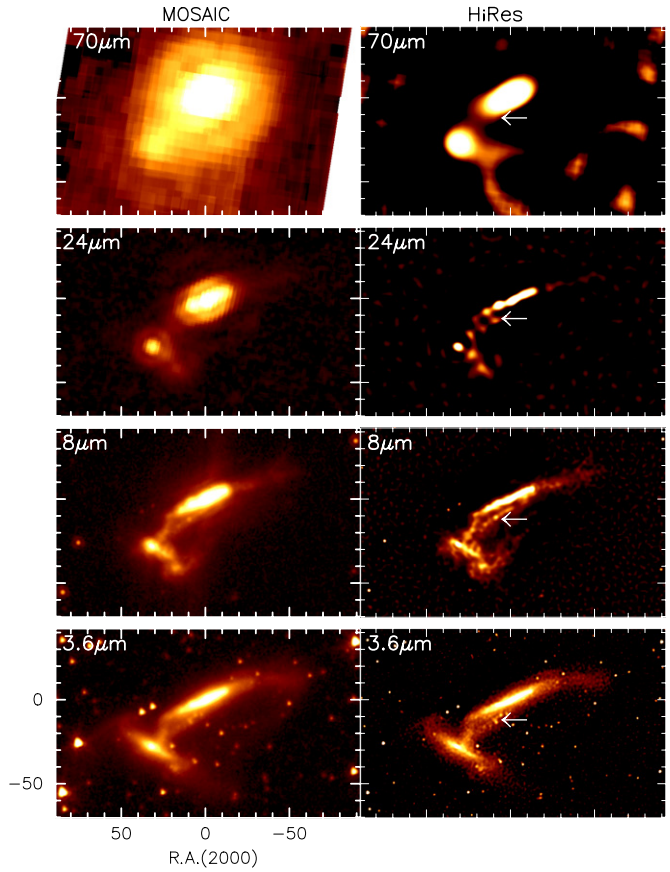


**Figure 18.** Interacting galaxies Arp 278. The white arrow marks the streamers.

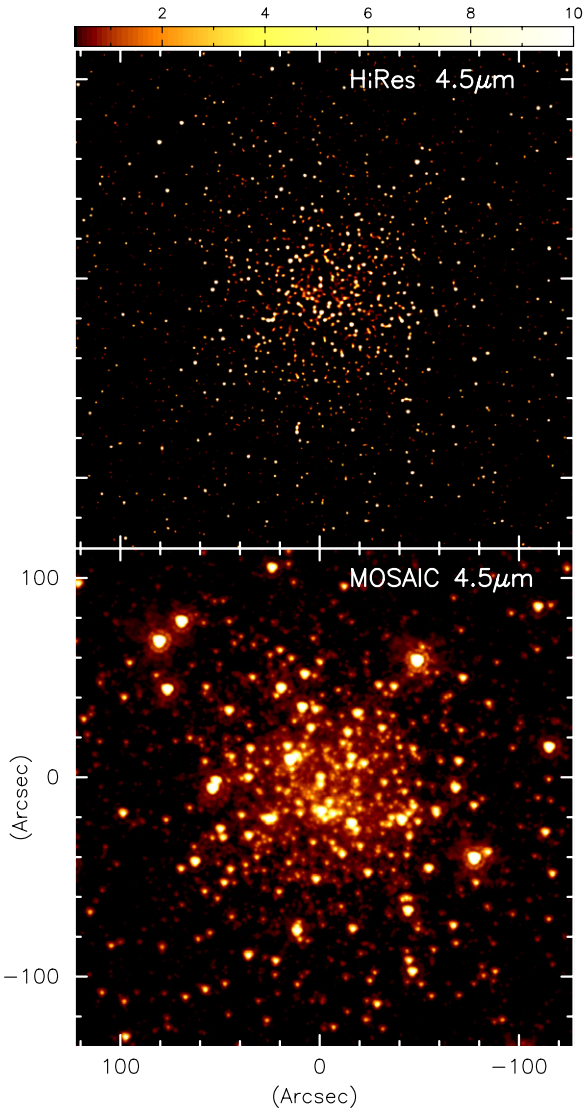


**Figure 19.** Images of globular cluster NGC 4590 at 4.5 $\mu$m.

(as marked in Figure 20). It may be interesting to apply HiRes on the star clusters (total 92) discovered in the GLIMPSE survey (Mercer et al. 2005). Deconvolution could greatly improve upon the distribution of cluster memberships.

### *4.8. Galactic Plane: G359.67+0.63*

The Galactic center region is unique in our Galaxy and permits a close-up view of objects and phenomena that are impossible to obtain anywhere else. Because of the high stellar density toward the Galactic center, GLIMPSE is confusion limited. It is severely limited by blending of fainter sources and by the diffraction lobes of bright sources. In the HiRes images the sources are better resolved, and better isolated from the residual diffraction lobes. Use of HiRes deconvolution provides a means of reducing confusion and enabling detection of fainter sources, thereby increasing the number of detections by factors of 3 to 4 in some of the most scientifically interesting regions. As a test case we processed one of the GLIMPSE II (see Meade et al. 2007) AORs imaging a $1.7^\circ \times 0.37^\circ$ field in the inner Galaxy. In Figure 21 we show the mosaic (made using the SSC BCDs) and HiRes images of a 10 $(\text{arcmin})^2$ region centered near G359.67+0.633 at 4.5 and 8 $\mu$m bands. These


**Figure 20.** IRAC three-color images of globular cluster NGC 4590: blue: 3.6 $\mu$m, green: 5.8 $\mu$m, red: 8 $\mu$m. The white arrow marks deblending of a giant star in the HiRes image (see the text).

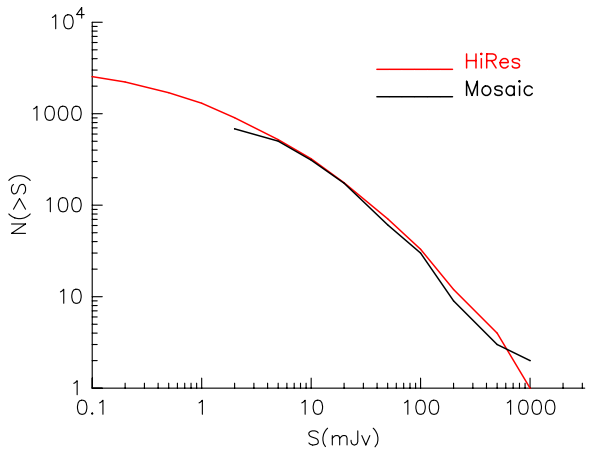


**Figure 22.** Source count in the IRAC 4.5 $\mu$m HiRes and mosaic images shown in Figure 21.

images demonstrate how HiRes resolves point sources well below the confusion limit in the mosaic images. Clearly we can see many more sources in the HiRes image that resemble noise in the mosaic. In fact SExtractor finds four times more sources above $5\sigma$ in the HiRes images than in the mosaic. Furthermore the presence of a bright source (saturated at 4.5 $\mu$m) and its associated effects such as "muxstriping" (8 $\mu$m) as seen in mosaic images has not affected HiRes performance in the adjacent areas of the images. In this particular example the diffraction lobes around the bright star are not cleaned well in the HiRes image because of the saturation.

In Figure 22 we show an example of the source count as extracted using SExtractor in a $5' \times 5'$ area around the region shown in Figure 21. The apparent excess of sources in the mosaic image at the highest flux is due to the blending of multiple

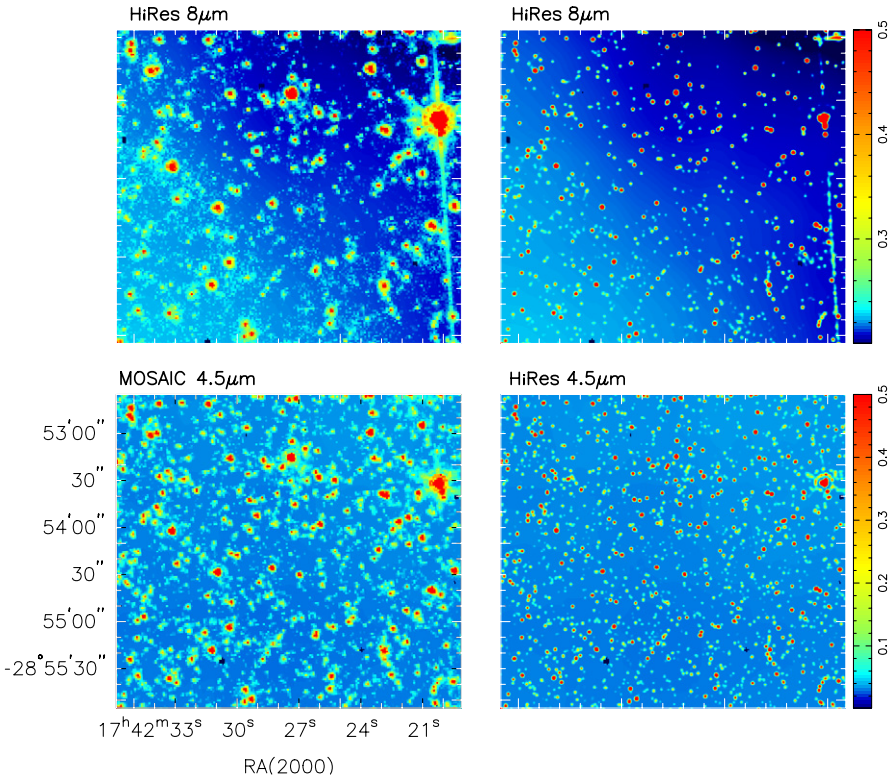


**Figure 21.** Example of HiRes of a GLIMPSE II AOR14302208 at position G359.67+0.633. The mosaic and HiRes images are shown with identical color stretches. The intensities are in mJy per 0.4″ pixel.

sources identified as single objects with a higher flux density while in the deconvolved image they are identified correctly with appropriate lower fluxes.

## 5. CONCLUSIONS

HiRes performs two functions: (1) it sweeps in the flux from the diffraction lobes into the main lobe; (2) it sharpens the main lobe resulting in a factor of 2 to 3 enhancement in resolution. To achieve this performance, care is necessary in the selection of the PRF, and also in the mitigation of data artifacts such as saturation, muxbleed, and muxstiping. The examples that we have presented demonstrate the effectiveness of HiRes deconvolution on *Spitzer* images and how it can provide enhanced science capabilities with *Spitzer* images. Our results demonstrate that the benefits of the resolution improvement include (i) an improved ability to show the spatial morphology of resolved sources; (ii) the ability to detect sources below the diffraction-limited confusion level; (iii) the ability to separate blended sources, and thereby provide guidance to point-source extraction procedures.

A choice of the number of iterations used for deconvolution allows a trade-off between resolution enhancement and ability to detect extended low-surface structures around bright sources. The ability to detect extended emission around very bright point sources is somewhat limited by the presence of diffraction residues caused by possible saturation effects at their peaks and any mismatch of the PRFs. The examples presented here provide some empirical experience to show deconvolution of *Spitzer* images can lead to reliable recovery of some of the small- and large-scale structures given the quality of data and the morphological complexity of the structures. It is useful to the extent that image sharpening makes interesting features more evident. We recognize HiRes deconvolution only as a useful technique and its application identifies interesting features for deeper analysis. By no means is it final and additional investigation, perhaps with least-squares analysis and modeling, will probably be required, independently of the deconvolution exercise.

The wide range of examples presented here is intended to give the readers some guidance as to where it is good to use HiRes and what improvements to expect. For example, in the 3.6 and 4.5 $\mu$m IRAC bands the protostellar outflows are traceable in the scattered light from the protostars. The examples given here and already published results have shown (and verified) detection outflow cones in the HiRes images of protostars that were completely hidden in the raw IRAC image. We recognize a solid niche for *Spitzer* observations in the study of outflow cones with IRAC data and use of deconvolution will enhance the feasibility of similar projects during the warm phase of *Spitzer*.

We thank the referee for useful comments, particularly in regard to comparison of *Spitzer* deconvolved images with high-spatial-resolution images. We also thank M. Ressler and Bo Reipurth for providing the Keck and *HST* NIRCAM FITS images. The research described in this paper was carried out at the Jet Propulsion Laboratory, California Institute of Technology, under a contract with the National Aeronautics and Space Administration. The HiRes work was supported by the Center for Long Wavelength Astrophysics in JPL. The authors thank C. Lawrence, W. Langer, and M. Werner for their help at various levels of this research.

## REFERENCES

Arce, H. G., & Sargent, A. I. 2006, ApJ, 646, 1070
Aumann, H. H., Fowler, J. W., & Melnyk, M. 1990, AJ, 99, 1674
Backus, C. R., Velusamy, T., Thompson, T. J., & Arballo, J. K. 2005, in ASP Conf. Ser. 347, ADASS XIV, ed. P. L. Shopbell, M. C. Britton, & R. Ebert (San Francisco, CA: ASP), 61
Blair, W. P., Ghavamian, P., Long, K. S., Williams, B. J., Borkowski, K. J., Reynolds, S. P., & Sankrit, R. 2007, ApJ, 662, 998
Cao, Yu, Terebey, S., Prince, T. A., & Beichman, C. A. 1997, ApJS, 111, 387
Cassam-Chenaï, G., Hughes, J. P., Ballet, J., & Decourchelle, A. 2007, ApJ, 665, 315
Condon, J. J., Cotton, W. D., Yin, Q. F., Shupe, D. L., Storrie-Lombardi, L. J., Helou, G., Soifer, B. T., & Werner, M. W. 2003, AJ, 125, 2411
Dempster, P., Laird, N. M., & Rubin, D. B. 1977, J. R. Stat. Soc. B, 39, 1
Elmegreen, D. M., Elmegreen, B. G., Kaufman, M., Sheth, K., Struck, C., Thomasson, M., & Brinks, E. 2006, ApJ, 642, 158
Frayer, D. T., et al. 2004, ApJS, 154, 137
Hurt, R. L., & Barsony, M. 1996, ApJ, 460, L45
Kalas, , et al. 2005, Nature, 435, 1067
Langer, W. D., Velusamy, T., & Thompson, T. J. 2007, BAAS, 38, 1203
Lee, J.-W., Carney, B. W., & Habgood, M. J. 2005, AJ, 129, 251
Lucy, L. B. 1974, AJ, 79, 745
Marsh, K. A., Velusamy, T., Dowell, C. D., Grogan, K., & Beichman, C. A. 2005, ApJ, 640, L47
Meade, M. R., et al. 2007, GLIMPSE II Data Products: v1, http://data.spitzer.caltech.edu/popular/glimpse2/2007Mar/documentation/
Mercer, E. P., et al. 2005, ApJ, 635, 560
Morganti, R., Garrett, M. A., Chapman, S., Baan, W., Helou, G., & Soifer, T. 2004, A&A, 424, 373
Neufeld, D. A., et al. 2006, ApJ, 649, 816
Noriega-Crespo, A., et al. 2004a, ApJS, 154, 352
Noriega-Crespo, A., et al. 2004b, ApJS, 154, 402
O'Linger, J., Wolf-Chase, G., Barsony, M., & Ward-Thompson, D. 1999, ApJ, 515, 695
Prasad, S. 2002, J. Opt. Soc. Am., 19, 7
Reipurth, B., Hartigan, P., Heathcote, S., Morse, J. A., & Bally, J. 1997, AJ, 114, 757
Reipurth, B., Yu, K., Heathcote, S., Bally, J., & Rodriguez, L. 2000, AJ, 120, 1449
Reipurth, B., Yu, K. C., Rodriguez, L. F., Heathcote, S., & Bally, J. 1999, A&A, 352, L83
Ressler, M. E., & Barsony, M. 2001, AJ, 121, 1098
Ressler, M. E., & Barsony, M. 2003, ApJ, 584, 832
Ressler, M. E., Werner, M. W., Van Cleve, J., & Chou, H. A. 1994, Exp. Astron., 3, 277
Richardson, W. H. 1972, J. Opt. Soc. Am., 62, 55
Stapelfeldt, K. R., et al. 2004, ApJS, 154, 458
Tobin, J. J., Looney, L. W., Mundy, L. G., Kwon, W., & Hamidouche, M. 2007, ApJ, 659, 1404
Velusamy, T., Langer, W. D., & Marsh, K. A. 2007a, ApJL, 668, L159
Velusamy, T., Langer, W. D., & Marsh, K. A. 2007b, BAAS, 39, 198
Warren, J. S., et al. 2005, ApJ, 634, 376
Waters, L. B. F. M., & Waelkens, C. 1998, ARA&A, 36, 233
Werner, M. W., et al. 2004, ApJS, 154, 1